Supporting Information

Efficient Electrochemical Water Oxidation to Hydrogen Peroxide over Intrinsic Carbon Defect-Rich Carbon Nanofibers

Yanhui Sun,[a] Xin Chen,[a] Shangbo Ning,[a] Wei Zhou,[b] Zhongshan Yang,[a] Jiwei Cui,[a] Defa Wang,[a] Jinhua Ye,[ac] and Lequan Liu*[a]

[a] TJU-NIMS International Collaboration Laboratory, Key Lab of Advanced Ceramics and Machining Technology (Ministry of Education) and Tianjin Key Laboratory of Composite and Functional Materials, School of Material Science and Engineering, Tianjin University, 92 Weijin Road, Tianjin 300072, P. R. China.

[b] Department of Applied Physics, Tianjin Key Laboratory of Low Dimensional Materials Physics and Preparing Technology, Faculty of Science, Tianjin University, Tianjin 30072, P. R. China.

[c] International Center for Materials Nanoarchitectonics (WPI-MANA), National Institute for Materials Science (NIMS), 1-1 Namiki, Tsukuba, Ibaraki 3050044, Japan.

Materials and Methods

Chemicals

All reagents were commercially available, of reagent grade, and used without further purification.

Synthesis of CNFs/NF.

The carbon nanofibers supported on 0.5 mm thick nickel foam (CNFs/NF) were prepared by chemical vapor deposition (CVD) method. As shown in Figure S1, NF was firstly heated to 600℃ at an increasing rate of 10 ℃/min and maintained for 120 min at a gas flow of 100 sccm mixed gases of Ar and H_2 (9/1; v/v). Then, the tubular furnace was introduced 100 sccm Ar instead of mixed gases of Ar and H_2 (9/1; v/v). After 30 min, 20 sccm acetylene (C_2H_2) was introduced in the chamber maintaining for 5 min. Finally, the sample was cooled down to room temperature. The CNFs/NF with different concentrations of intrinsic carbon defects was obtained by adjusting growth temperatures of CNFs for 500, 550, 650 and 700℃, termed as CNFs/NF-500, CNFs/NF-550, CNFs/NF-650, CNFs/NF-700, respectively. In addition, NF was subjected to same treatment at 600℃ without introducing C_2H_2, denoted as NF.

Synthesis of CNFs/NF@PTFE.

The CNF/NF-600 and NF were soaked into 60% (30%) PTFE aqueous solution for 10 min and then dried at 70℃ in a vacuum oven. Note that the 30% PTFE solutions were diluted from 60% PTFE. Then, the samples were annealed at 350°C under Ar atmosphere for 30 min, denoted as CNFs/NF@PTFE-60% (30%), NF@PTFE-60%, respectively.

Synthesis of control samples.

In order to exclude the influence of Ni, CNFs/NF-600 was calcinated at 600°C under air atmosphere for 180 min to obtain the oxidized sample, denoted as O-CNFs/NF. O-CNFs/NF was calcinated at 600°C under mixed gases of Ar and H_2 (9/1; v/v) atmosphere for 180 min to obtain reduced sample, denoted as R-O-CNFs/NF. CNFs/CoF was parpared by replacing nickel foam with cobalt foam.

Characterization.

The XRD patterns were recorded by an X-ray diffractometer (Cu Kα radiation, D8 Advanced, Bruker, Germany). The morphologies of samples were observed by field-emission scanning electron microscope (FE-SEM) (S-4800, Hitachi, Japan) and high-resolution transmission electron microscopy (HRTEM) (Tecnai G2 F30 FEI, U.S.A.). Raman analysis was recorded on a Raman microscope with an incident wavelength of 532 nm (Raman, HORIBA Scientific, Japan). X-ray photoelectron spectroscopy (XPS) studies were carried out on Thermo ESCALAB 250Xi, where C 1s (284.6 eV) was used as a reference to correct the binding energy. Near edge X-ray absorption fine structure (NEXAFS) spectroscopy measurements were carried out on the soft X-ray spectroscopy beamline at the Singapore Synchrotron Radiation Facility.

Electrochemical measurements.

The electrochemical measurements were conducted in a customized H-type electrolytic cell separated by Nafion 117 membrane. The $2e^-$-WOR performance were investigated by using an electrochemical station (CHI760E, CHI instrument) with the three-electrode configuration. The CNFs/NF-x, Ag/AgCl (3.0 M KCl) and platinum foil were used as the working electrode, reference electrode and counter electrode, respectively. Unless otherwise noted in this study,1.0 M Na_2CO_3 solution was used as the electrolyte (PH=11.83) with a volume of 100 ml in each compartment. The electrolyte in the anodic compartment was stirred at a rate of 1,000 r.p.m and the temperature of that was kept at 280K by controlled by a thermostatic water bath. Note that 4 mg ml^{-1} Na_2SiO_3 was added into the anodic electrolyte to stabilize H_2O_2 produced during current-time chronoamperometric testing. The concentration of accumulated H_2O_2 was quantified by Fe^{2+}/ Fe^{3+} method using ultraviolet-visible (UV-vis) and cross-validated with N, N-diethyl-1,4-phenylene-diamine (DPD) method. The Fe^{2+}/ Fe^{3+} method is that 0.1 mL of 0.1 M $FeCl_2$ in 1.0 M HCl was added to a mixed solution containing 0.5 mL of electrolyte, 0.5 ml deionized water and 0.9 mL of 3.0 M HCl solution. The H_2O_2 concentration was then measured by Fe^{3+} colorimetry (330 nm), according to the following equation:

$$Fe^{2+} + H_2O_2 \rightarrow Fe^{3+} + 2OH^- \quad (S1)$$

Typically, the DPD and the peroxidase (POD) solution was prepared by dissolving 0.1 g DPD and 10 mg POD in 10 mL 0.1 N H_2SO_4 solution and 10 mL deionized water, respectively, and then stored in the refrigerator. 6 g monobasic potassium phosphate and 1.4 g dipotassium phosphate was dissolved in 100 ml of deionized water to prepare a phosphate buffer solution. The neutralized electrolyte (2 mL) was mixed with 0.8 mL phosphate buffer solution, 2.24 mL water, 0.1 mL DPD and 0.1 mL POD, and then measured by UV-vis spectroscopy. As shown in the Figure S5, the measured results by the above two methods are basically the same. Unless otherwise specified, the generated H_2O_2 in this work was detected using Fe^{2+}/Fe^{3+} method.

It should be noted that purchased hydrogen peroxide (*w*=30%) should be calibrated as hydrogen peroxide is easily decomposed. In this work, we calibrated the concentration of the newly purchased hydrogen peroxide by potassium permanganate titration method. A typical titration process is: (1) Calibration of 0.02 M potassium permanganate standard solution by sodium oxalate ($Na_2C_2O_4$). (2) The concentration of newly purchased hydrogen peroxide (*w*=30%) is calibrated by potassium permanganate. The experimental details are shown in Supplementary Table S1.

The FE for H_2O_2 production (%) is calculated using the following equation:

$$FE = \frac{\text{generated } H_2O_2 \text{ (mol)} \times 2 \times 96485}{\text{total amount of charge passed (C)}} \times 100\% \quad (S2)$$

The electrochemically active surface areas (ECSAs) were studied by the electrochemical double-layer capacitance (C_{dl}) of electrocatalysts at non-faradaic potentials. C_{dl} values were calculated from cyclic voltammetry measurements (CV) which were cycled between -0.1 to 0 V vs Ag/AgCl at different scan rates.

For the carbon nanotubes and graphite measurements, 5 mg of electrocatalyst, 1000 μL of ethanol and 15 μL of 5wt% Nafion solution were mixed together and sonicated for 30 min to make the catalyst uniformly dispersed. Then 150 uL of catalyst ink was evenly dropped on the surface of the NF electrode and dried at room temperature.

Computational methods.

In this work, first-principles calculations based on density functional theory (DFT) were performed using the Vienna Ab Initio Simulation Package (VASP). And the generalized gradient approximation with Perdew-Burke-Ernzerhof (GGA-PBE) was used to describe the exchange-correlation interactions. The plane wave cutoff energy was set as 400 eV. For geometry optimization, the convergences of force and energy were set to 0.02 eV $Å^{-1}$ and 1×10^{-5} eV, respectively. A 16 Å vacuum thickness was adopted to avoid the interactions between adjacent structures. For armchair and zigzag defects, all edge carbon atoms were saturated with hydrogen to eliminate dangling bonds. The Monkhorst-Pack k-point grids were: 3 × 3 × 1 for pristine, 1 × 2 × 1 for armchair, 3 × 1 × 1 for zigzag, 2 × 1 × 1 for octagon and pentagon models.

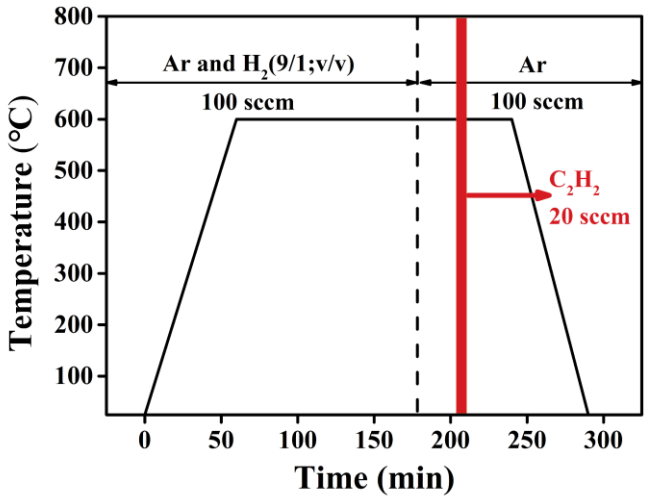

Figure S1. Time dependence of experimental parameters: temperature, gas composition and gas flow rates.

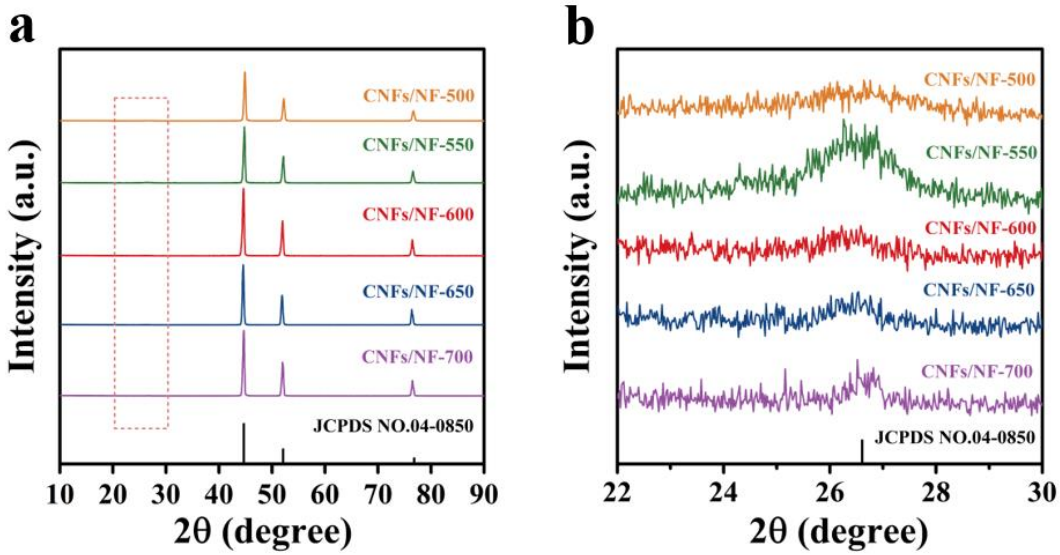

Figure S2. XRD pattern of CNFs/NF-x. The image of **b** is an enlarged view of the frame line in **a**.

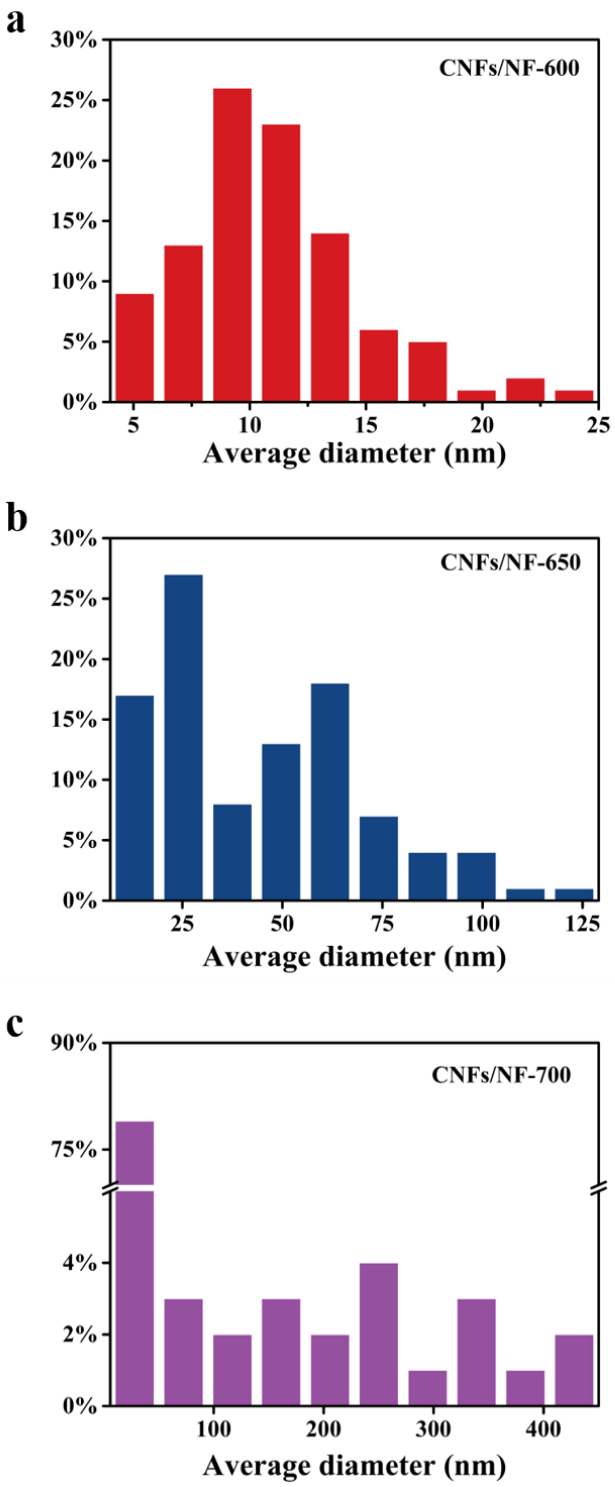

Figure S3. The diameter distributions of CNFs/NF-x (x=600, 650 and 700).

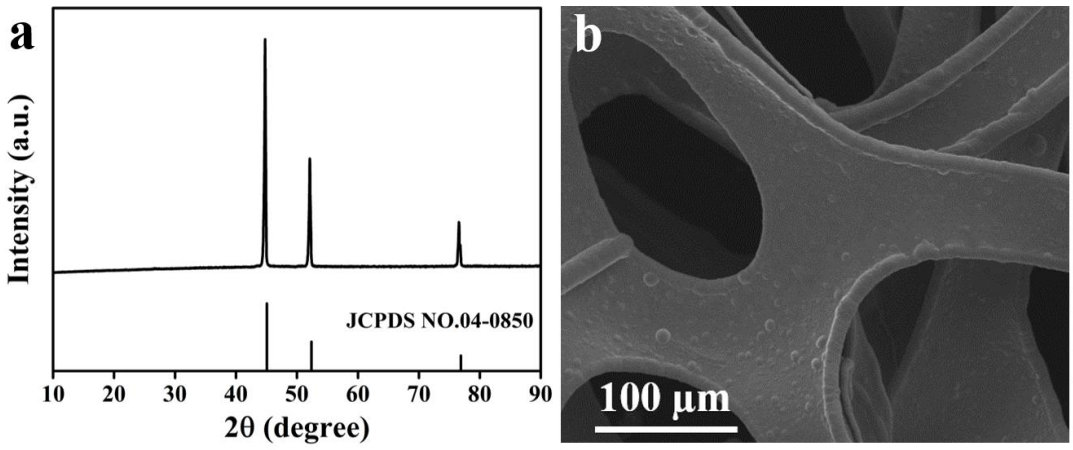

Figure S4. Structural characterizations of NF. **a**, XRD pattern. **b**, SEM image.

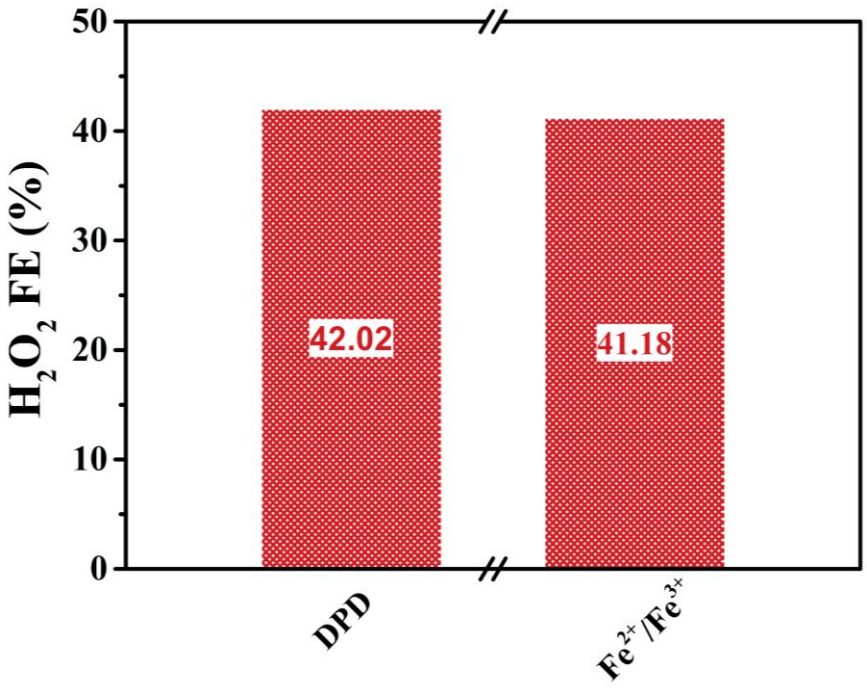

Figure S5. The concentration of accumulated H_2O_2 quantified by DPD and Fe^{2+}/Fe^{3+} methods, respectively.

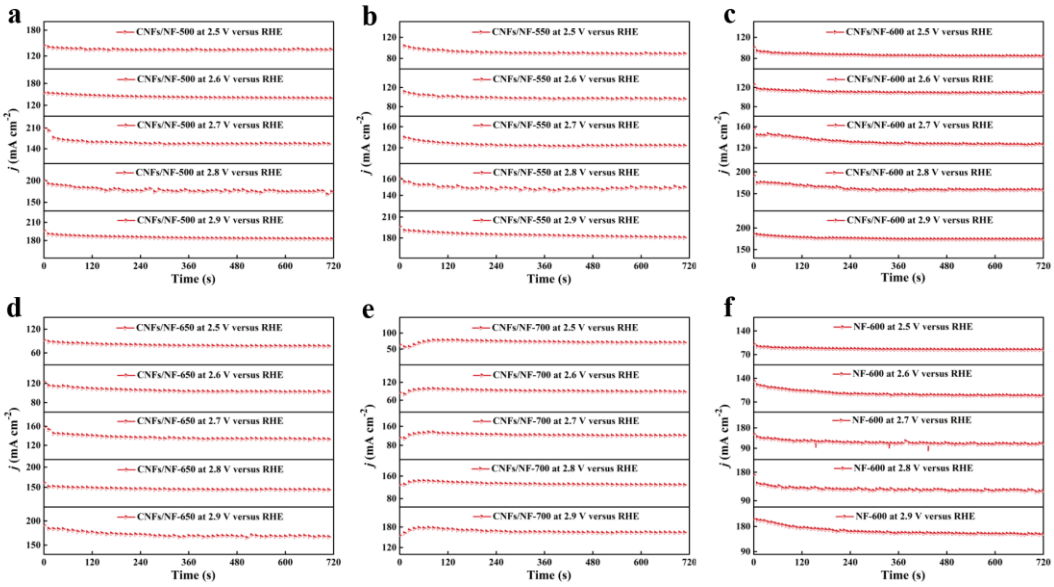

Figure S6. Current density records of NF and CNFs/NF-x during 2e$^-$-WOR evaluation under different applied potentials.

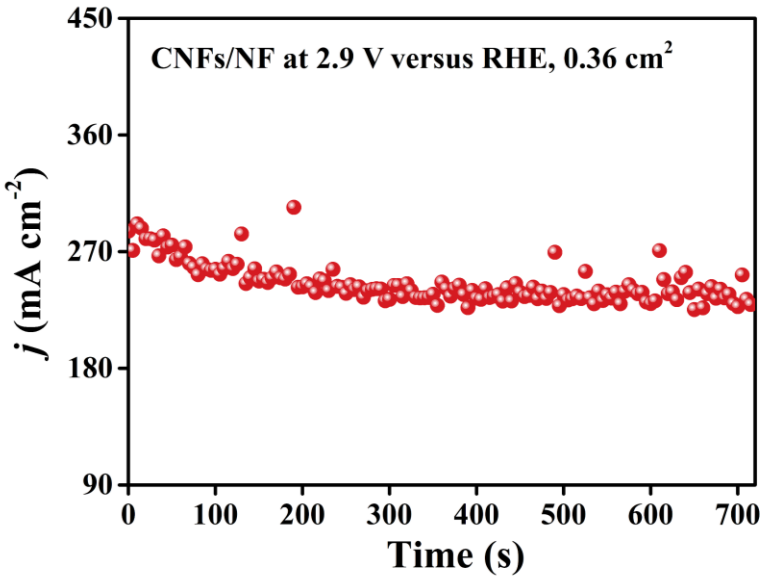

Figure S7. Current density records of CNFs/NF-600 during 2e$^-$-WOR evaluation under 2.9 V vs RHE. The geometric area of the immersed electrode is 0.36 cm^2.

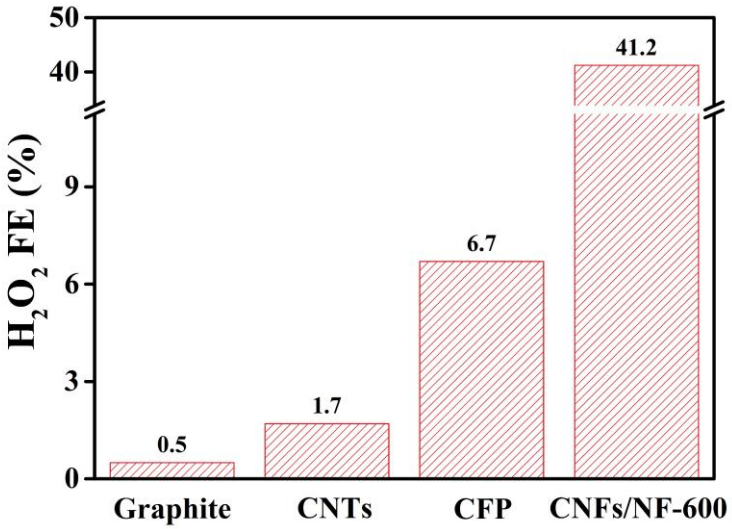

Figure S8. The H_2O_2 FE of CFP, CNTs, graphite and CNFs/NF-600 at 2.9 V vs RHE.

In order to study whether the morphology of nanofiber play a role in promoting the performance of $2e^-$-WOR, the electrocatalytic evaluation of commercial carbon fiber paper (CFP), carbon nanotubes (CNTs) and graphite for $2e^-$-WOR were carried out. As shown in Figure S8, CFP showed higher H_2O_2 FE (6.7%) compared with CNTs and graphite, yet lower than 41.2% FE of CNFs/NF. Therefore, though the morphology of nanofibers slightly promotes the H_2O_2 production, the main role for the improved $2e^-$-WOR performance should be the intrinsic carbon defect.

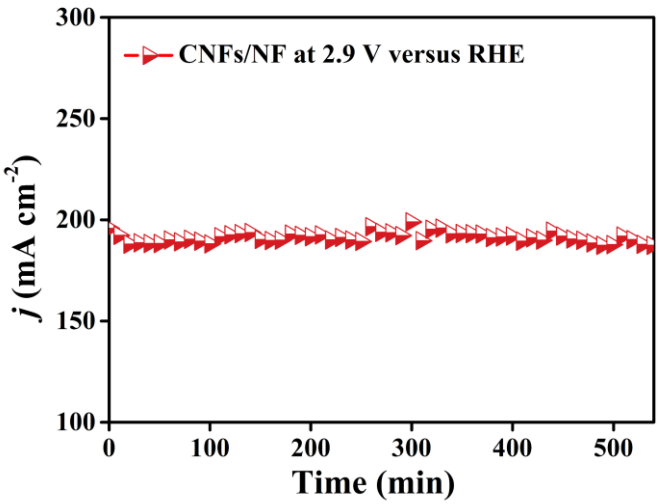

Figure S9. Stability test result for CNFs/NF-600 under 2.9 V vs RHE.

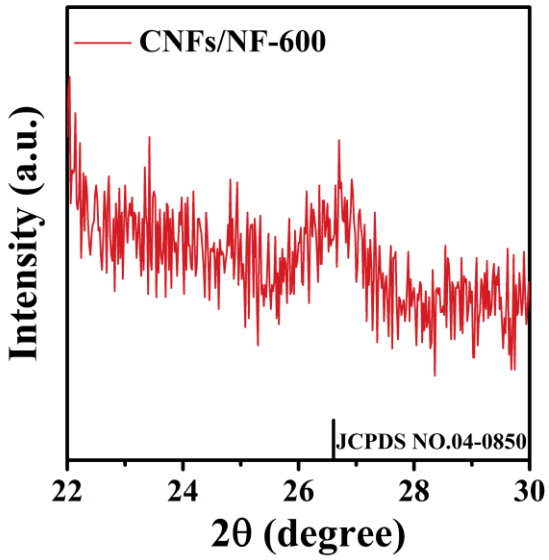

Figure S10. XRD pattern of CNFs/NF-600 after stability test.

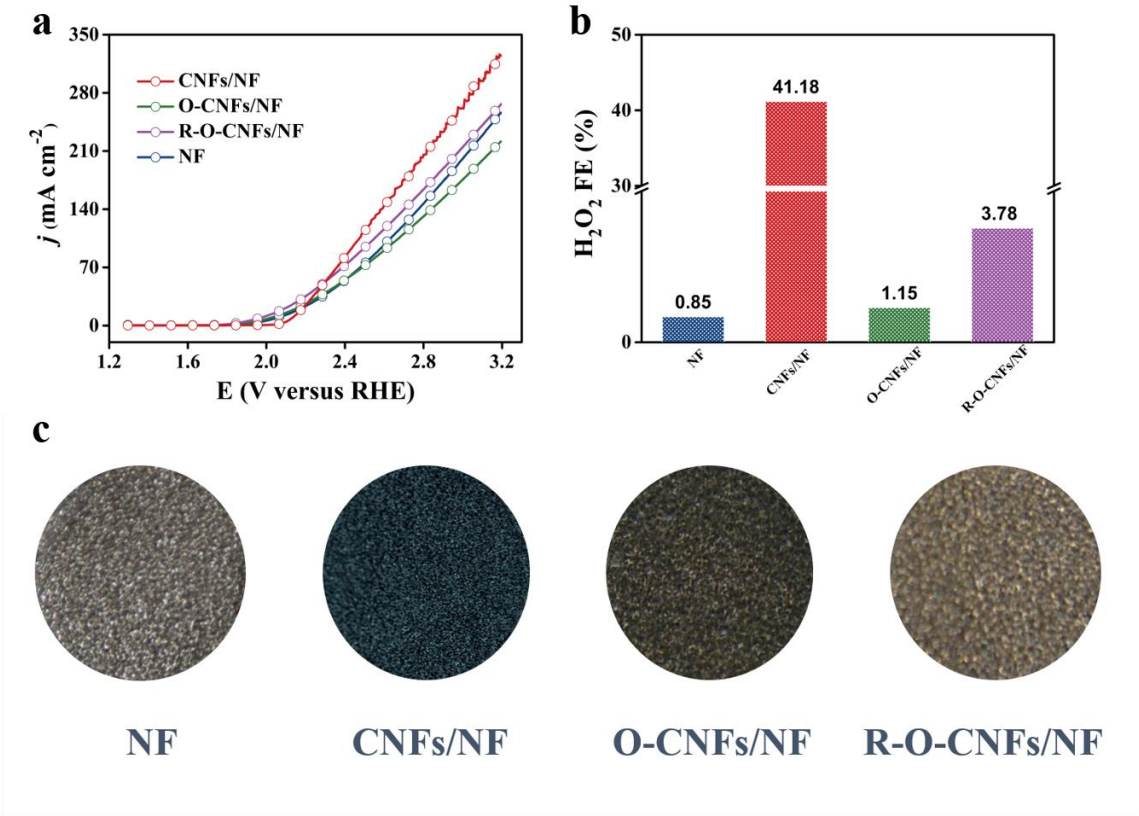

Figure S11. a, The linear sweep voltammetry curve (LSV) of NF, CNFs/NF, O-CNF/NF and R-O-CNFs/NF. **b**, FE of H_2O_2 on NF, CNFs/NF, O-CNF/NF and R-O-CNFs/NF at 2.9V vs RHE. **c,** digital photos of NF, CNFs/NF, O-CNFs/NF and R-O-CNFs/NF.

In order to explore the influence of Ni in CNFs, exploratory experiments were carried out and CNFs/NF mentioned below refer to CNFs/NF-600. First, the defective CNFs supported on NF was removed to obtain O-CNFs/NF by high-temperature oxidation in a muffle furnace. Next, the O-CNFs/NF was reduced under mixed gases of Ar and H_2 (9/1; v/v) atmosphere to form R-O-CNFs/NF (Methods). As shown in Figures S11a, c, it can be seen that removing defective CNFs will reduce the current density and generate black-green nickel oxide (NiO) with poor conductivity. Compared to O-CNFs/NF, R-O-CNFs/NF enhance current density due to the removal of NiO on the surface. Figure S11b shows that the FE for H_2O_2 production of NF, CNFs/NF, O-CNF/NF, R-O-CNFs/NF under 2.9 V vs RHE are 0.85%, 41.2%, 1.15%, 3.78%,

respectively. Remarkably, the H_2O_2 FE of the O-CNFs/NF and R-O-CNFs/NF was rapidly lower than that of CNFs/NF, which suggest intrinsic carbon defects in CNFs play a vital role in $2e^-$-WOR. Furthermore, the Ni coated by CNFs is not the main reason to change the water oxidation reaction path, because the redox treatment only removes CNFs without changing Ni.

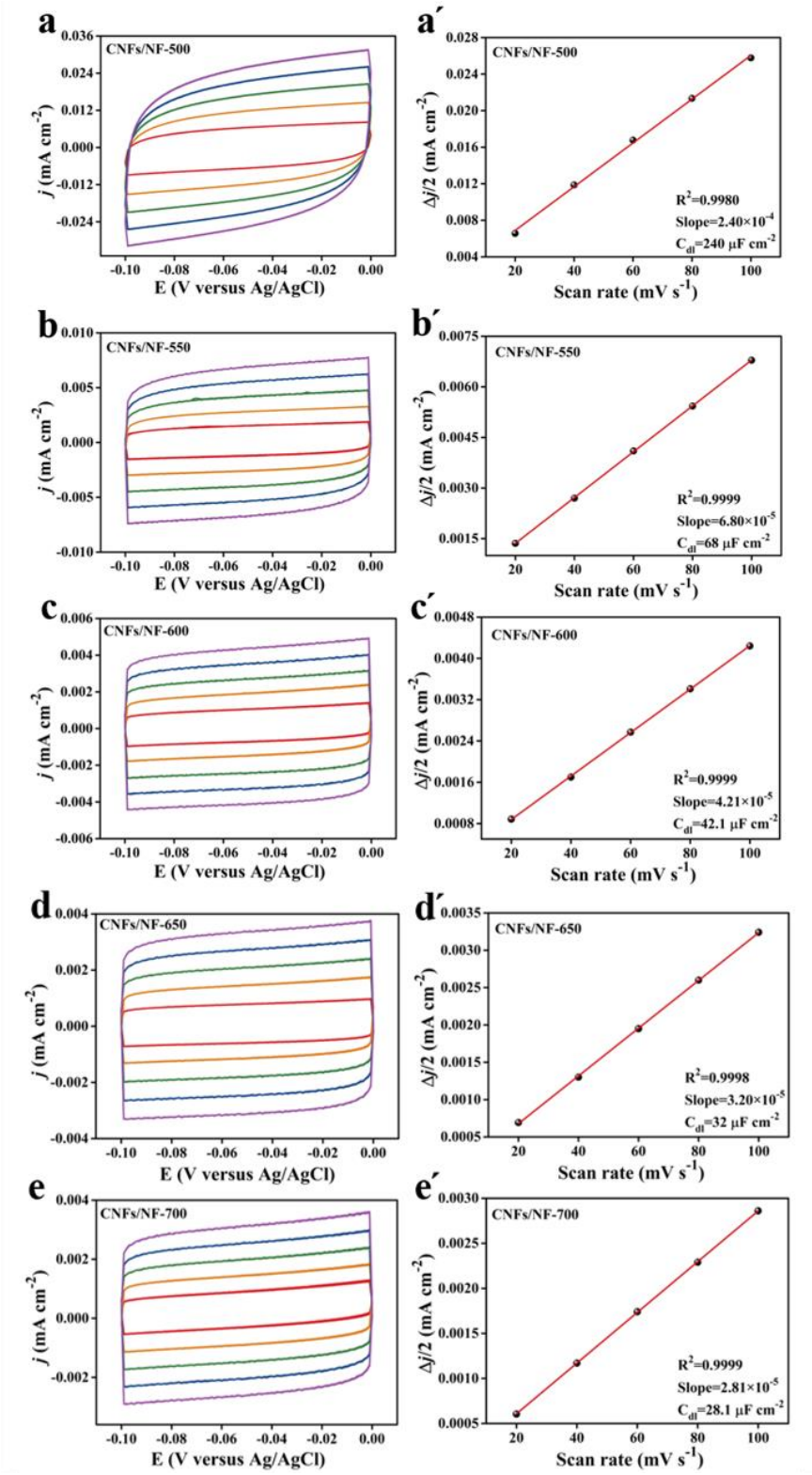

Figure S12. Double-layer capacitance measurements for CNFs/NF-x. **a-a′**, CNFs/NF-500. **b-b′**, CNFs/NF-550. **c-c′**, CNFs/NF-600. **d-d′**, CNFs/NF-650. **e-e′**, CNFs/NF-700.

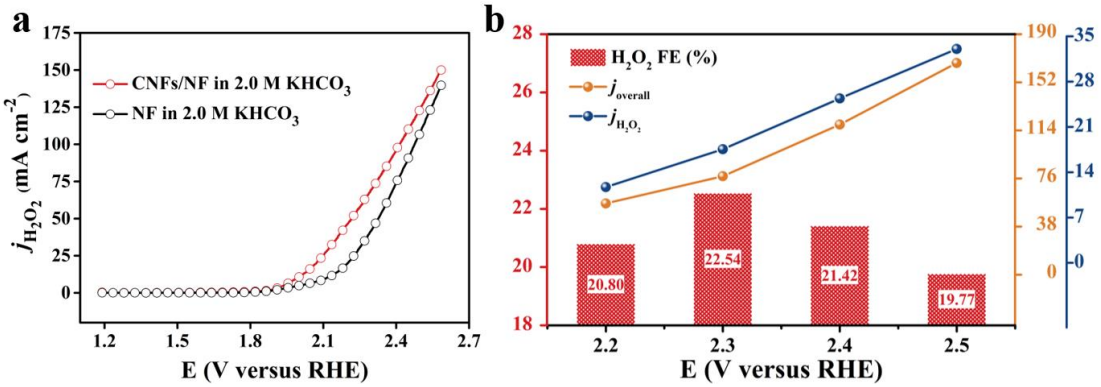

Figure S13. $2e^-$-WOR performances of CNFs/NF-600 and NF in 2 M $KHCO_3$ electrolyte (pH=8.30). **a**, LSV of CNFs/NF-600 and NF. **b**, The H_2O_2 FE, average current density and partial current density for CNFs/NF-600.

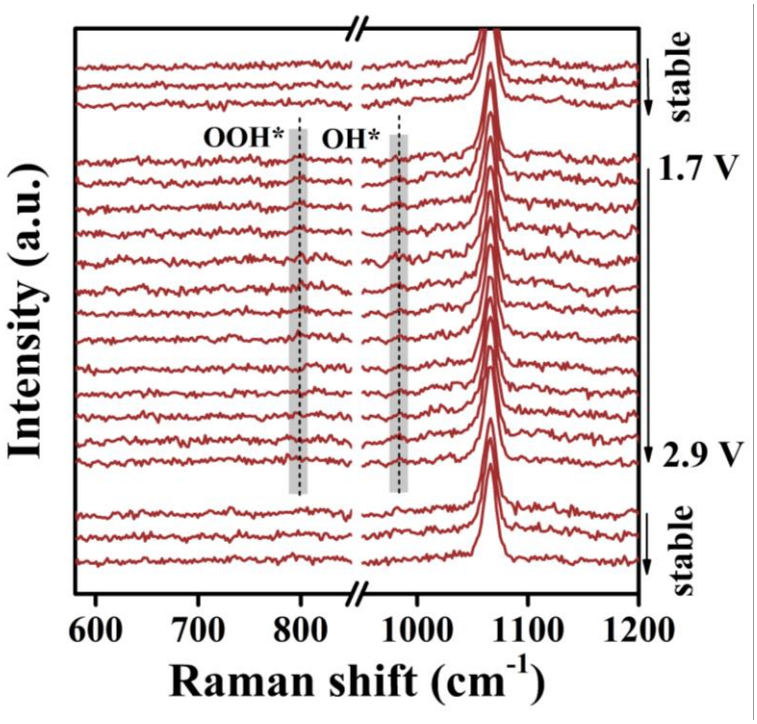

Figure S14. Enlarged view of Figure 2f.

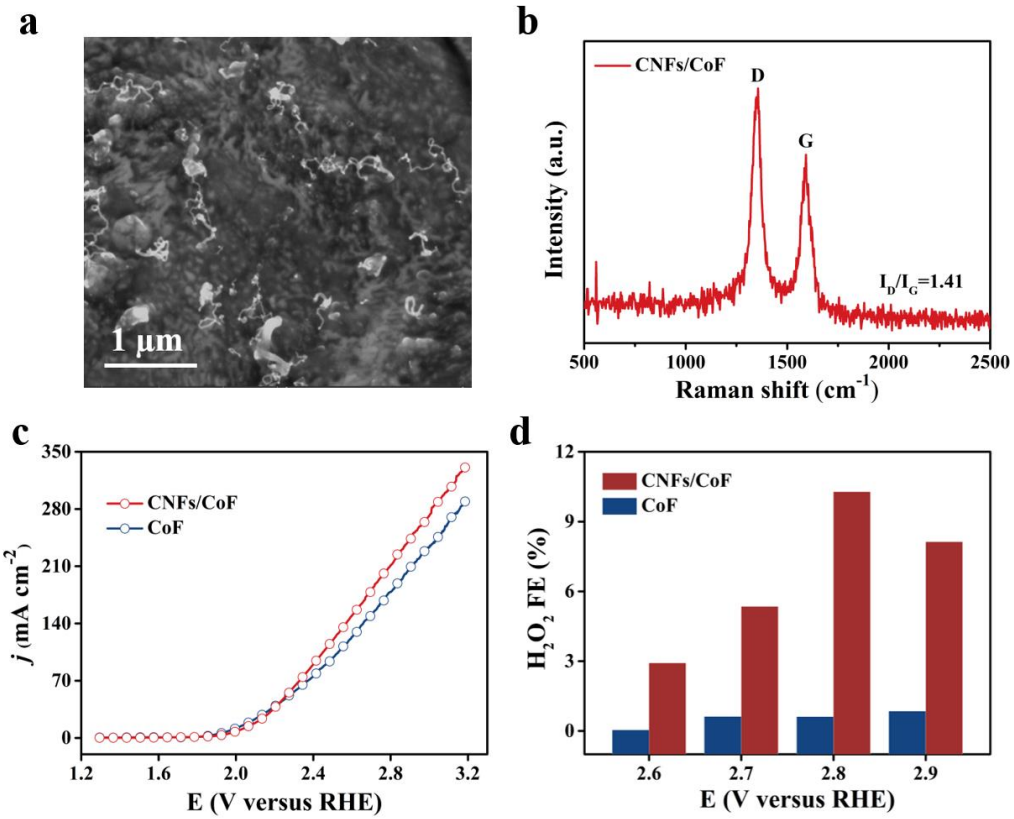

Figure S15. a, SEM image of CNFs/CoF. **b,** The Raman spectra of CNFs/CoF. **c,** The LSV of CNFs/CoF and CoF. **d,** The H_2O_2 FE of CNFs/CoF and CoF.

The CNFs with rich intrinsic carbon defects can be successfully extended to cobalt foam (CNFs/CoF). SEM characterization and Raman spectra suggest successful growth of defective CNFs over CoF (I_D/I_G=1.41), **Figure S15a, b**. The H_2O_2 FE of 10.3% was achieved over CNFs/CoF at 2.8 V vs RHE, except for enhanced H_2O_2 current density (21.71 mA cm^{-2}) compared with CoF, **Figure S15c, d**. Therefore, this controlled synthesis of carbon materials with intrinsic carbon defects provides guidance towards the design of future carbon-based catalysts for the electrochemical production of H_2O_2.

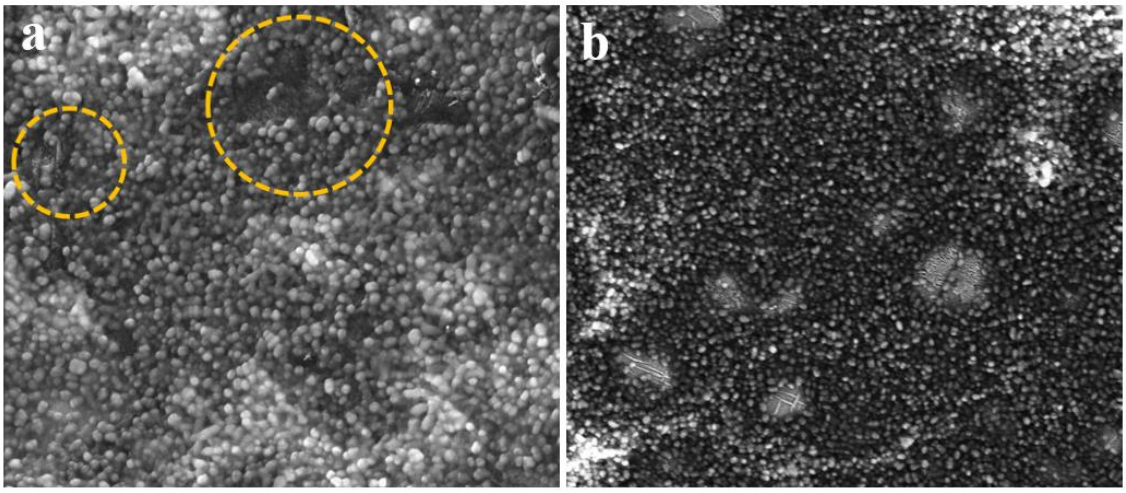

Figure S16. a, SEM image of CNFs/NF@PTFE-60%. **b**, SEM image of NF@PTFE-60%.

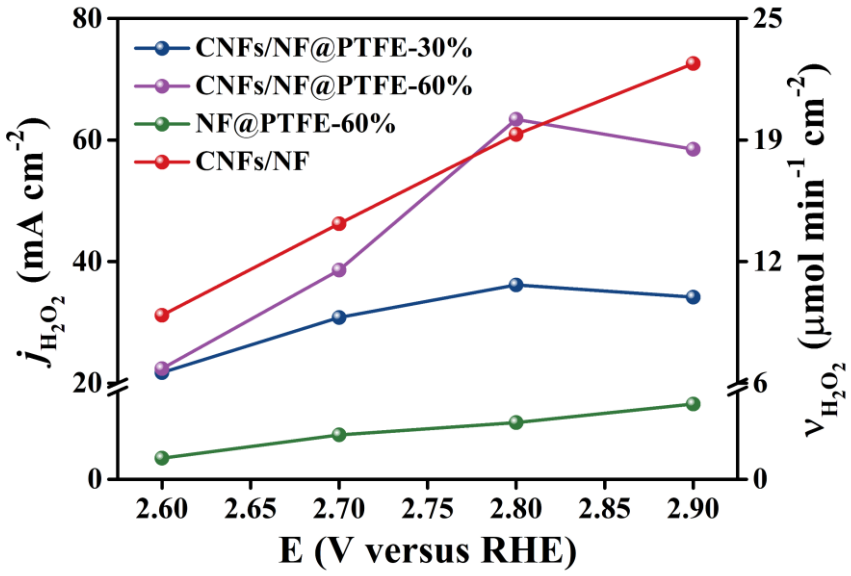

Figure S17, H_2O_2 current density and generation rates of CNFs/NF@PTFE-x, NF@PTFE-60% and CNFs/NF under different applied potentials.

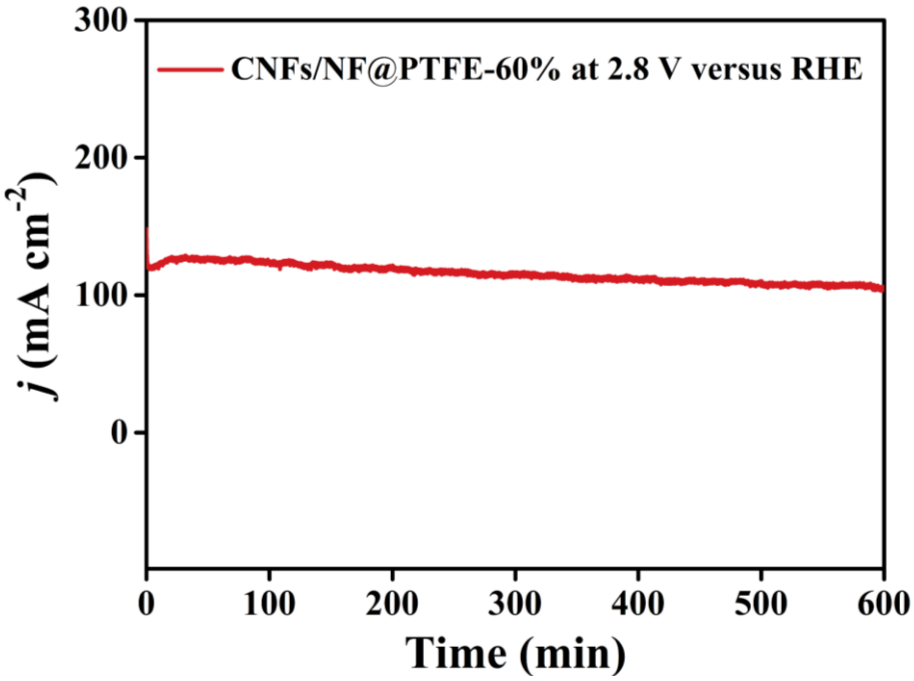

Figure S18. Stability test result for CNFs/NF@PTFE-60% under 2.8 V versus RHE.

Table S1. Calibration of the newly purchased H_2O_2 concentration (*w*=30%) by potassium permanganate titration.

Calibration of prepared potassium permanganate solution

Number of titrations	1	2	3	4
Mass: $Na_2C_2O_4$ (g)	0.1985	0.1669	0.1768	0.1546
Volume: $KMnO_4$ (ml)	31	26	26	23.6
Concentration: $KMnO_4$ (mol/L)	0.0191	0.0192	0.020	0.0196
Average Concentration $KMnO_4$ (mol/L)	0.0195			

Calibration of newly purchased hydrogen peroxide

Volume: H_2O_2 (ml)	25	15	10
Volume: $KMnO_4$ (ml)	40.2	24.4	16.3
Concentration: H_2O_2 (mol/L)	30.29%	30.64%	30.70%
Average Concentration H_2O_2 (mol/L)	30.54%		

Table S2. Summary of electrocatalytic water oxidation for H_2O_2 production.

Electrocatalyst	Potenial vs RHE	$J_{H_2O_2}$ (mA cm^{-2})	$FE_{H_2O_2}$	v (μmol min^{-1} cm^{-2})	Immersion Area	Electrolyte	Ref.
Al_2O_3/FTO	-	-	-	≈0.12	13.2 cm^2	0.5 M $KHCO_3$	1
$BiVO_4$/FTO	-	-	-	≈0.54	13.2 cm^2	0.5 M $KHCO_3$	1
BDD	3.5 V	≈63.4	28%	19.7	7.4 cm^2	2.0 M $KHCO_3$	2
$CaSnO_3$/FTO	3.2 V	≈15.1	76%	4.7	-	2.0 M $KHCO_3$	3
CPF	2.4 V	75.2	66%	23.4	0.36 cm^2	1.0 M Na_2CO_3	4
$CaSnO_3$@CF	2.9 V	≈94.5	90%	39.8	-	1.0 M Na_2CO_3	5
InSbOx/$CuSb_2$Ox	-	≈3.5	53%	-	6 cm^2	$KHCO_3$	6
ZnO/FTO	2.6 V	≈13.1	81%	-	-	2.0 M $KHCO_3$	7
$BiVO_4$/FTO	3.1 V	≈19	70%	5.9	1 cm^2	1.0 M $NaHCO_3$	8
SnO_2/FTO	3.1 V	≈5.1	50%	1.6	1 cm^2	1.0 M $NaHCO_3$	8
WO_3/FTO	2.25 V	≈1.9	48%	0.6	1cm^2	1.0 M $NaHCO_3$	8
TiO_2/FTO	3.3 V	≈3.2	20%	1	1 cm^2	1.0 M $NaHCO_3$	8
C,N codoped TiO_2	≈3.3 V	≈0.9	8%	0.29	-	0.05 M Na_2SO_4	9
CNFs/NF-600	2.9 V	72.6	41.2%	22.6	1 cm^2	1.0 M Na_2CO_3	**This work**
CNFs/NF@PTFE	2.9 V	63.4	53.8%	19.7	1cm^2	1.0 M Na_2CO_3	**This work**

Table S3. The curve fitting results of C1s XPS spectra (CNFs/NF-500 and CNFs/NF-600).

	Area 1 (C-C sp^2)	Area 2 (C-C sp^3)	Area 2/Area1
CNFs/NF-500	29816.44	6036.25	0.202
CNFs/NF-600	39678.93	6585.72	0.166

References

1 K. Fuku, Y. Miyase, Y. Miseki, T. Gunji and K. Sayama, *Chemistryselect*, 2016, **1**, 5721-5726.

2 S. Mavrikis, M. Goltz, S. Rosiwal, L. Wang and C. P. de Leon, *Acs Appl Energ Mater*, 2020, **3**, 3169-3173.

3 S. Y. Park, H. Abroshan, X. J. Shi, H. S. Jung, S. Siahrostami and X. L. Zheng, *Acs Energy Letters*, 2019, **4**, 352-357.

4 C. Xia, S. Back, S. Ringe, K. Jiang, F. Chen, X. Sun, S. Siahrostami, K. Chan and H. Wang, *Nature Catalysis*, 2020, **3**, 125-134.

5 C. Q. Zhang, R. H. Lu, C. Liu, L. Yuan, J. Wang, Y. Zhao and C. Z. Yu, *Adv Funct Mater*, 2021, 2100099.

6 Y. Miyase, Y. Miseki, T. Gunji and K. Sayama, *Chemelectrochem*, 2020, **7**, 2448-2455.

7 S. R. Kelly, X. J. Shi, S. Back, L. Vallez, S. Y. Park, S. Siahrostami, X. L. Zheng and J. K. Norskov, *Acs Catal*, 2019, **9**, 4593-4599.

8 X. J. Shi, S. Siahrostami, G. L. Li, Y. R. Zhang, P. Chakthranont, F. Studt, T. F. Jaramillo, X. L. Zheng and J. K. Norskov, *Nat Commun*, 2017, **8**, 701.

9 S. G. Xue, L. Tang, Y. K. Tang, C. X. Li, M. L. Li, J. J. Zhou, W. Chen, F. Zhu and J. Jiang, *Acs Appl Mater Inter*, 2020, **12**, 4423-4431.